

# $\alpha$ -Imaging Confirmed Efficient Targeting of CD45-Positive Cells After $^{211}\text{At}$ -Radioimmunotherapy for Hematopoietic Cell Transplantation

Sofia H.L. Frost<sup>1</sup>, Brian W. Miller<sup>2,3</sup>, Tom A. Bäck<sup>4</sup>, Erlinda B. Santos<sup>1</sup>, Donald K. Hamlin<sup>5</sup>, Sue E. Knoblaugh<sup>6</sup>, Shani L. Frayo<sup>1</sup>, Aimee L. Kenoyer<sup>1</sup>, Rainer Storb<sup>1,7</sup>, Oliver W. Press<sup>1,7</sup>, D. Scott Wilbur<sup>5</sup>, John M. Pagel<sup>1,7</sup>, and Brenda M. Sandmaier<sup>1,7</sup>

<sup>1</sup>Clinical Research Division, Fred Hutchinson Cancer Research Center, Seattle, Washington; <sup>2</sup>Pacific Northwest National Laboratory, Richland, Washington; <sup>3</sup>College of Optical Sciences, University of Arizona, Tucson, Arizona; <sup>4</sup>Sahlgrenska Academy, University of Gothenburg, Gothenburg, Sweden; <sup>5</sup>Department of Radiation Oncology, University of Washington, Seattle, Washington; <sup>6</sup>Comparative Medicine Shared Resource, Fred Hutchinson Cancer Research Center, Seattle, Washington; and <sup>7</sup>Department of Medicine, University of Washington, Seattle, Washington

$\alpha$ -radioimmunotherapy targeting CD45 may substitute for total-body irradiation in hematopoietic cell transplantation (HCT) preparative regimens for lymphoma. Our goal was to optimize the anti-CD45 monoclonal antibody (mAb; CA12.10C12) protein dose for  $^{211}\text{At}$ -radioimmunotherapy, extending the analysis to include intraorgan  $^{211}\text{At}$  activity distribution and  $\alpha$ -imaging-based small-scale dosimetry, along with immunohistochemical staining.

**Methods:** Eight normal dogs were injected with either a 0.75 ( $n = 5$ ) or 1.00 ( $n = 3$ ) mg/kg dose of  $^{211}\text{At}$ -B10-CA12.10C12 (11.5–27.6 MBq/kg). Two were euthanized and necropsied 19–22 h after injection, and 6 received autologous HCT 3 d after  $^{211}\text{At}$ -radioimmunotherapy, after lymph node and bone marrow biopsies at 2–4 and/or 19 h after injection. Blood was sampled to study toxicity and clearance; CD45 targeting was evaluated by flow cytometry.  $^{211}\text{At}$  localization and small-scale dosimetry were assessed using two  $\alpha$ -imaging systems: an  $\alpha$ -camera and an ionizing-radiation quantum imaging detector (iQID) camera. **Results:**  $^{211}\text{At}$  uptake was highest in the spleen (0.31–0.61% injected activity [%IA]/g), lymph nodes (0.02–0.16 %IA/g), liver (0.11–0.12 %IA/g), and marrow (0.06–0.08 %IA/g). Lymphocytes in blood and marrow were efficiently targeted using either mAb dose. Lymph nodes remained unsaturated but displayed targeted  $^{211}\text{At}$  localization in T lymphocyte-rich areas. Absorbed doses to blood, marrow, and lymph nodes were estimated at 3.1, 2.4, and 3.4 Gy/166 MBq, respectively. All transplanted dogs experienced transient hepatic toxicity. Liver enzyme levels were temporarily elevated in 5 of 6 dogs; one treated with 1.00 mg mAb/kg developed ascites and was euthanized 136 d after HCT. **Conclusion:**  $^{211}\text{At}$ -anti-CD45 radioimmunotherapy with 0.75 mg mAb/kg efficiently targeted blood and marrow without severe toxicity. Dosimetry calculations and observed radiation-induced effects indicated that sufficient  $^{211}\text{At}$ -B10-CA12.10C12 localization was achieved for efficient conditioning for HCT.

**Key Words:** radioimmunotherapy;  $^{211}\text{At}$ ; alpha imaging; CD45; lymphoma

**J Nucl Med 2015; 56:1766–1773**

DOI: 10.2967/jnumed.115.162388

**H**ematopoietic cell transplantation (HCT) is a curative treatment option for many malignant and nonmalignant hematologic disorders. A key element is the HCT conditioning regimen, which prevents relapse after remission by reducing the underlying disease burden and facilitates allogeneic engraftment through host immunosuppression. In recent years, efforts have been made to increase the absorbed dose to target sites while reducing the radiation-induced adverse effects, through substitution of radiolabeled monoclonal antibodies (mAbs) for standard pretreatment total-body  $\gamma$ -irradiation. The radioimmunotherapy regimens have generally used  $\beta$ -emitters such as  $^{131}\text{I}$ , which are suboptimal for killing hematopoietic cells because of their long particle range and low linear energy transfer. Conversely, short-ranged  $\alpha$ -emitters deposit very high energies over a few cell diameters (40–100  $\mu\text{m}$ ), making  $\alpha$ -radioimmunotherapy an appealing option for improving the specificity and efficacy of conditioning (1).

Our group has previously explored  $\alpha$ -radioimmunotherapy preparative regimens for HCT in preclinical models, concluding that conditioning with either  $^{213}\text{Bi}$ - or  $^{211}\text{At}$ -anti-CD45-radioimmunoconjugates was efficacious, without significant nonhematopoietic toxicity (2–5).  $^{211}\text{At}$  was chosen over  $^{213}\text{Bi}$  for subsequent  $\alpha$ -radioimmunotherapy studies because of its superior myelosuppression, lower cost, greater availability, and clinically less challenging half-life (7.2 h for  $^{211}\text{At}$  vs. 46 min for  $^{213}\text{Bi}$ ).

CD45 is a cell surface tyrosine phosphatase that regulates T-cell and B-cell activation and maturation. It is broadly expressed ( $\sim 200,000$  copies per cell) on all hematopoietic cells except platelets and erythrocytes, regardless of malignant transformation (6). Our overall goal is to achieve efficient targeting and pharmacokinetics with minimal normal-tissue toxicity using  $^{211}\text{At}$ -anti-CD45-radioimmunoconjugates to replace total-body irradiation or high-dose chemotherapy conditioning in HCT preparative regimens for hematopoietic diseases. In this study, we aimed to optimize the

Received Jun. 16, 2015; revision accepted Aug. 20, 2015.

For correspondence or reprints contact: Sofia H.L. Frost, Fred Hutchinson Cancer Research Center, 1100 Fairview Ave. N., P.O. Box 19024, Seattle, WA 98109-1024.

E-mail: sfrost@fredhutch.org

Published online Sep. 3, 2015.

COPYRIGHT © 2015 by the Society of Nuclear Medicine and Molecular Imaging, Inc.

anti-CD45 mAb protein dose in a canine model, evaluating the results through blood counts, plasma chemistry, flow cytometry, immunohistochemical staining,  $\alpha$ -imaging, and small-scale  $\alpha$ -dosimetry.

## MATERIALS AND METHODS

### Antibodies and Antibody Conjugates

Anticanine CD45 mAb CA12.10C12 (2,3,5,7) was conjugated with *closo*-decaborate(2-) to produce CA12.10C12-B10 for  $^{211}\text{At}$ -labeling, as previously described (8). Flow cytometry was performed as described by Sandmaier et al. (2). mAbs were produced and purified at the Biologics Production Facility at Fred Hutchinson Cancer Research Center (FHCRC).

### Radioactivity

$^{211}\text{At}$  was produced using a MC-50 cyclotron (Scanditronix) at the University of Washington and isolated through a wet-chemistry method (8). Subsequent  $^{211}\text{At}$ -labeling of CA12.10C12-B10 was performed using the procedure of Chen et al. (5). All radioactive materials were handled according to approved protocols at FHCRC and the University of Washington.

### Dogs

The dogs were raised at FHCRC and given standard immunizations. The experimental protocol was approved by the FHCRC Institutional Animal Care and Use Committee, and the study was executed according to principles outlined in the *Guide for the Care and Use of Laboratory Animals* (9).

### Flow Cytometry

Surface-bound anti-CD45 was detected through flow cytometry of cell suspensions prepared from samples of blood, lymph nodes, and bone marrow aspirates, as previously described (2,5). Antigen saturation was determined by comparing the mean fluorescence intensity of cells incubated with either fluorescein isothiocyanate-conjugated goat antimouse F(ab')<sub>2</sub> (FMF) or fluorescein isothiocyanate-conjugated anti-CD45 mAb (CD45F).

### Biodistribution, Pharmacokinetics, and Toxicity

Two anti-CD45 mAb dose levels (0.75 mg/kg,  $n = 5$ ; 1.00 mg/kg,  $n = 3$ ) were evaluated with regard to in vivo distribution, pharmacokinetics, and normal-organ toxicity. The starting level was based on previous canine studies, which showed that 0.50 mg/kg insufficiently

saturated available CD45 antigens (2,3,5). Unlabeled CA12.10C12 (0.05 mg/kg) was injected 30–60 min before  $^{211}\text{At}$ -mAb infusion to prevent nonspecific Fc receptor binding. Clearance of mAb and  $^{211}\text{At}$  was assessed using blood collected from 5 min before to 22 h after radioimmunoconjugate injection, using an enzyme-linked immunosorbent assay as previously described (2) and by radioactivity measurements, respectively. Eight dogs were infused with CA12.10C12-B10 labeled with 14.6–36.7 MBq  $^{211}\text{At}$ /mg mAb (Table 1); two were euthanized and necropsied without HCT 19–22 h after injection. Harvested tissues were weighed and measured for radioactivity, and the results were expressed as percentage injected activity (%IA) per gram after corrections for background and decay. Six dogs received autologous HCT 3 d after the  $^{211}\text{At}$ -mAb infusion. Marrow was aspirated from humeri and femora at least 2 wk before radioimmunotherapy and then processed and stored as previously described (10,11). Biopsies of lymph nodes and bone marrow were taken at an early (2–4 h) and/or a late (19–22 h) time point after  $^{211}\text{At}$ -mAb infusion. Samples were split for flow analysis,  $\alpha$ -imaging, immunohistochemistry, and radioactivity measurement.

Toxicities were evaluated by measuring complete blood counts, blood urea nitrogen, creatinine, and liver enzymes at baseline, daily for the first 2 mo or until full hematopoietic recovery, and then weekly until the end of the study. Necropsies at euthanasia included gross examination and tissue harvesting for pathologic assessment of microscopic abnormalities.

### $\alpha$ -Imaging

Two  $\alpha$ -imaging systems were used for high-resolution ex vivo assessment of  $^{211}\text{At}$  localization and microdosimetry: an  $\alpha$ -camera (12) and an ionizing-radiation quantum imaging detector (iQID) camera (13). Cryosections (10–12  $\mu\text{m}$ ) of popliteal lymph nodes and bone marrow cores were placed on a scintillation film (EJ-440; Eljen Technology) and imaged as previously described (14). Consecutive sections were stained with hematoxylin and eosin (H&E) for histological comparison with the imaged intraorgan  $^{211}\text{At}$  distribution.

### Dosimetry

Absorbed doses to blood were estimated individually from the blood samples by creating time-activity curves (%IA/g as a function of time) assuming 100 %IA in blood at injection ( $t = 0$ ). Blood volumes were derived from individual dog weights and a standardized total blood volume of 102.6 mL/kg (15). The cumulated  $^{211}\text{At}$  activity ( $\bar{A}$ ) was calculated after exponential curve fitting for each time-activity

**TABLE 1**  
Dogs Treated with  $^{211}\text{At}$ -Anti-CD45 Radioimmunotherapy

Dog no.	Age (mo)	Weight (kg)	mAb dose* (mg/kg)	$^{211}\text{At}$ activity (MBq/kg)	Specific $^{211}\text{At}$ activity (MBq/mg mAb)	Autologous transplant	Sample time (h after injection)	Transfusions (d after HCT)	Survival (wk)
H573	12	7.7	0.75	14.6	19.5	No	22	—	—
H585	9	9.4	0.75	27.6	36.7	No	19	—	—
H543	20	12.8	0.75	11.5	15.3	Yes	19	7, 11, 19	48†
H689	7	8.7	0.75	13.9	18.5	Yes	2, 19	7	32†
H522	22	11.8	0.75	13.9	18.6	Yes	2	8	46†
H629	8	9.5	1.00	14.6	14.6	Yes	2, 19	6, 8, 12	20‡
H638	10	12.3	1.00	18.4	18.4	Yes	4, 19	6, 10, 14, 16, 19, 22	32†
H632	10	8.4	1.00	18.7	18.7	Yes	2, 19	7, 9	32†

\*Including 0.05 mg/kg of unlabeled mAb.

†End of study.

‡Severe ascites.

curve. Using an absorbed fraction of  $\alpha$ -particles ( $\Phi_\alpha$ ) of 1 and including contributions exclusively from  $\alpha$ -particles, the absorbed dose ( $D$ ) in Gy was calculated using the equation

$$D = \frac{\tilde{A}}{m} \Delta_\alpha \Phi_\alpha,$$

where  $m$  denotes tissue mass in kilograms and  $\Delta_\alpha$  is the mean energy released per  $^{211}\text{At}$  decay ( $1.09 \times 10^{-12}$  J). Mean absorbed dose rates at biopsy were calculated and normalized to the individual injected activities ( $\mu\text{Gy}/\text{MBq}\cdot\text{s}$ ) for bone marrow (core and aspirate) and lymph nodes using radioactivity measurements of the samples. Total absorbed doses ( $\text{Gy}/\text{MBq}$ ) to marrow were estimated by interpolation between early and late time points using polynomial curve fits of the time–activity curves, assuming zero tissue radioactivity at  $t = 0$ .

Small-scale dosimetry was performed for marrow and lymph nodes through quantification of the radioactivity concentration ( $\text{Bq}/\text{g}$ ) at biopsy in the  $\alpha$ -imaged samples. Individual section masses were estimated using the area and thickness of each imaged section and a tissue density of  $1 \text{ g}/\text{cm}^3$ . Small-scale mean absorbed dose rates were calculated as described above and compared with those calculated for “macroscopic” (i.e., nonsectioned) biopsies using traditional whole-tissue dosimetry methods (16). Dose rate differences between various subcompartments in  $\alpha$ -imaged samples were also examined.

Image-based small-scale 3-dimensional dosimetry was performed for lymph nodes from 2 dogs, using voxel dose-point kernels and  $\alpha$ -camera imaging of serial sections (17). Briefly, series of 13 consecutive  $12\text{-}\mu\text{m}$  sections were imaged, registered, and stacked to a 3-dimensional matrix of  $12 \times 12 \times 12 \mu\text{m}^3$  voxels. Voxel dose-point kernels for  $^{211}\text{At}$  were generated using Monte Carlo simulation and convolved with the radioactivity images using MATLAB (The MathWorks, Inc.) to estimate the absorbed dose rate in each voxel. Dose rate distribution maps were thereby achieved for the centermost section (7/13) of each series.

### Histology and Immunohistochemistry

Formalin-fixed, paraffin-embedded lymph node samples were stained on a BOND RX system (Leica) with antibodies against CD3 (3  $\mu\text{g}/\text{mL}$ , MCA1477; Serotec), MAC 387 (0.2  $\mu\text{g}/\text{mL}$ , M0747; Dako), and cleaved caspase-3 (0.3  $\mu\text{g}/\text{mL}$ , CP229B; Biocare Medical) after ethylenediaminetetraacetic acid–based antigen retrieval. The CD3 antibody was followed by a rabbit antirat secondary, and all antibodies were then detected and visualized using Power Vision HRP polymers and Refine DAB (Leica Biosystems). The slides were scanned using an Aperio AT scanscope system (Leica) with  $\times 40$  image capture magnification and analyzed using the ImageScope viewing software.

## RESULTS

### $^{211}\text{At}$ -B10-CA12.10C12

Astatination of CA12.10C12-B10 was achieved with 74%–91% labeling yields. The radiochemical purity of the  $^{211}\text{At}$ -B10-CA12.10C12 was always greater than 98%, as determined by radio–high-performance liquid chromatography or instant thin-layer chromatography.

### Biodistribution and Pharmacokinetics

The in vivo distributions in selected tissues from nontransplanted dogs (H573 and H585) are shown in Figure 1A. The  $^{211}\text{At}$  accumulation was highest in lymphocyte-rich target tissues such as spleen (0.31–0.61 %IA/g), lymph nodes (0.02–0.16 %IA/g), and bone marrow core (0.06–0.08 %IA/g), and in the liver (0.11–0.12 %IA/g). Uptake levels in other tissues were low. The activity concentration

in bone marrow core for all dogs, at 1 or 2 biopsy time points, revealed no distinct trend in terms of accumulation or release over time (paired  $t$  test,  $P = 0.61$ ). Clearance of circulating  $^{211}\text{At}$  from blood is shown in Figure 1B. The mean %IA/g did not vary significantly between the 2 mAb doses (unpaired  $t$  test,  $P = 0.62$ ), whereas the mean anti-CD45 mAb concentration in plasma was higher for 1.00 mg/kg ( $P = 0.01$ ; Supplemental Fig. 1; supplemental materials are available at <http://jnm.snmjournals.org>).

### Anti-CD45 Saturation

Flow cytometry data for lymphocytes in marrow and lymph nodes are summarized in Tables 2 and 3, showing the mean fluorescence intensity and the relative percentage of FMF and CD45F staining, respectively. Bone marrow lymphocytes were rapidly and efficiently targeted by anti-CD45 mAb, as demonstrated by high intensity and percentage binding of FMF at the early time points. The corresponding CD45F numbers were low, indicating near saturation of CD45. In contrast, FMF staining of lymph node samples resulted in a low mean fluorescence intensity regardless of time point or mAb dose. This result, in combination with high CD45F intensity, confirmed the abundance of free antigen.

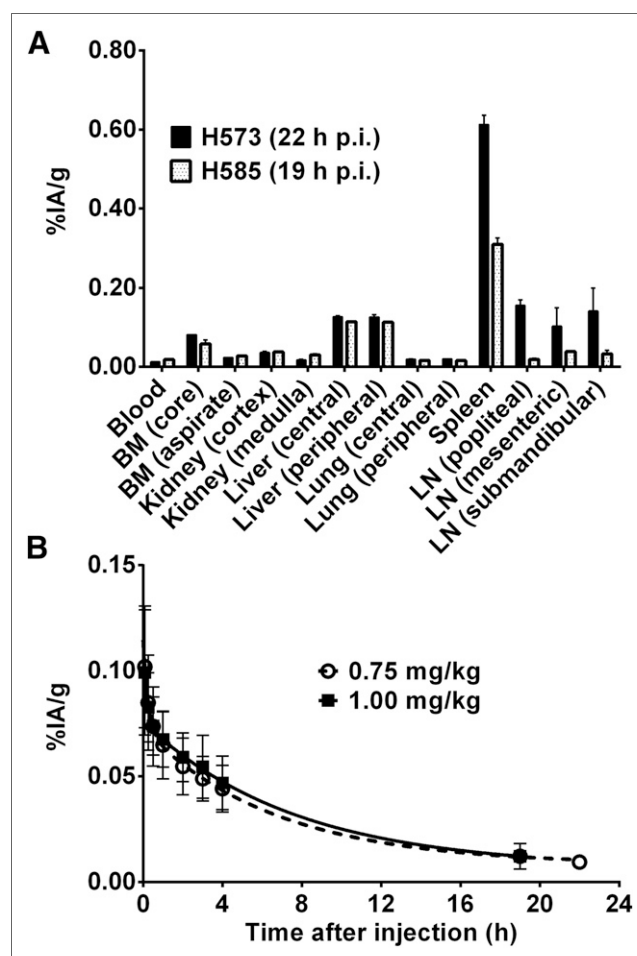


**FIGURE 1.** Biodistribution and clearance of  $^{211}\text{At}$ -anti-CD45 mAb. (A) Radioactive content expressed as %IA/g  $\pm$  SD ( $n = 3$ ) in selected tissues from 2 dogs euthanized 19–22 h after injection. (B) Retention of  $^{211}\text{At}$  in blood for all treated dogs, determined by radioactivity measurements of repeated blood samples (%IA/g  $\pm$  SD, 0.75 mg/kg,  $n = 5$ ; 1.00 mg/kg,  $n = 3$ ). p.i. = after injection.

**TABLE 2**  
Mean Fluorescence Intensity after Staining of CD45+ Cells (Gated on Lymphocytes)

Dog no.	Bone marrow core				Lymph node			
	FMF		CD45F		FMF		CD45F	
	2–4 h	19–22 h	2–4 h	19–22 h	2–4 h	19–22 h	2–4 h	19–22 h
H573*	—	7,245	—	1,292	—	1,288	—	7,500
H585*	—	1,009	—	213	—	402	—	7,027
H543*	—	17,931	—	669	—	2,358	—	5,257
H689*	28,172	10,082	553	1,841	2,178	1,011	12,133	6,020
H522*	10,432	—	82	—	505	—	6,935	—
H629†	17,956	1,000	109	65	758	2,774	6,041	6,025
H638†	37,176	32,831	220	548	1,780	1,057	15,113	13,754
H632†	24,298	38,886	155	564	1,517	4,478	14,112	17,067

\*mAb dose, 0.75 mg/kg.

†mAb dose, 1.00 mg/kg.

Flow cytometry dot plots of fluorescein isothiocyanate versus forward scatter indicated cell depletion in marrow at the later time point, but no similar effect was seen for lymph nodes. The antigen binding differed significantly in terms of FMF and CD45F mean fluorescence intensity in blood lymphocytes after  $^{211}\text{At}$ -mAb infusion, confirming the efficient saturation of CD45 sites on circulating lymphocytes (Supplemental Fig. 2).

#### $\alpha$ -Imaging

Images acquired using the  $\alpha$ -camera and the iQID camera showed heterogeneous  $^{211}\text{At}$  distribution in lymph nodes at all time points, with predominant localization to T lymphocyte-rich regions in the paracortex, as determined from consecutive H&E-stained cryosections (Fig. 2 and Supplemental Fig. 3). The lymph node medulla and follicles in the superficial cortex contained little radioactivity. Follicles in the superficial cortex presented as clearly defined dark, round areas in contrast to the high-intensity deep

cortical units (Figs. 2A and 2C). Quantitative image analysis showed that the activity concentrations in high-activity lymph node regions could be a factor of 8 up to 65 times higher than those in lower-activity regions. Apart from the bone matrix, which exhibited no quantifiable activity uptake, the marrow samples displayed a more homogeneous uptake profile at both time points, with high levels of  $^{211}\text{At}$  activity in all regions containing hematopoietic cells (Figs. 2B and 2D).

#### Histopathology and Immunohistochemistry

Visual examination of H&E slides and corresponding  $\alpha$ -images revealed an apparent association between apoptotic cells and high-signal areas, particularly at the later time points. Radiation-induced damage and associated features (cellular debris and macrophage infiltration) were distinctly increased in lymph nodes biopsied at 19 h after injection. Immunohistochemical staining of paraffin-embedded lymph nodes allowed more detailed analysis

**TABLE 3**  
Percentage of Stained CD45+ Cells (Gated on Lymphocytes)

Dog no.	Bone marrow core				Lymph node			
	FMF		CD45F		FMF		CD45F	
	2–4 h	19–22 h	2–4 h	19–22 h	2–4 h	19–22 h	2–4 h	19–22 h
H573*	—	44.7	—	51.0	—	9.9	—	97.0
H585*	—	13.7	—	6.1	—	2.7	—	98.2
H543*	—	94.2	—	15.2	—	17.2	—	82.4
H689*	95.8	81.7	11.7	87.8	8.0	10.0	93.7	96.8
H522*	91.4	—	0.4	—	4.2	—	97.0	—
H629†	95.6	5.2	0.1	0.8	5.4	24.4	94.1	88.3
H638†	97.2	92.8	0.8	5.3	6.8	6.8	96.8	97.2
H632†	78.9	93.6	0.5	7.5	6.2	35.8	97.9	97.9

\*mAb dose, 0.75 mg/kg.

†mAb dose, 1.00 mg/kg.

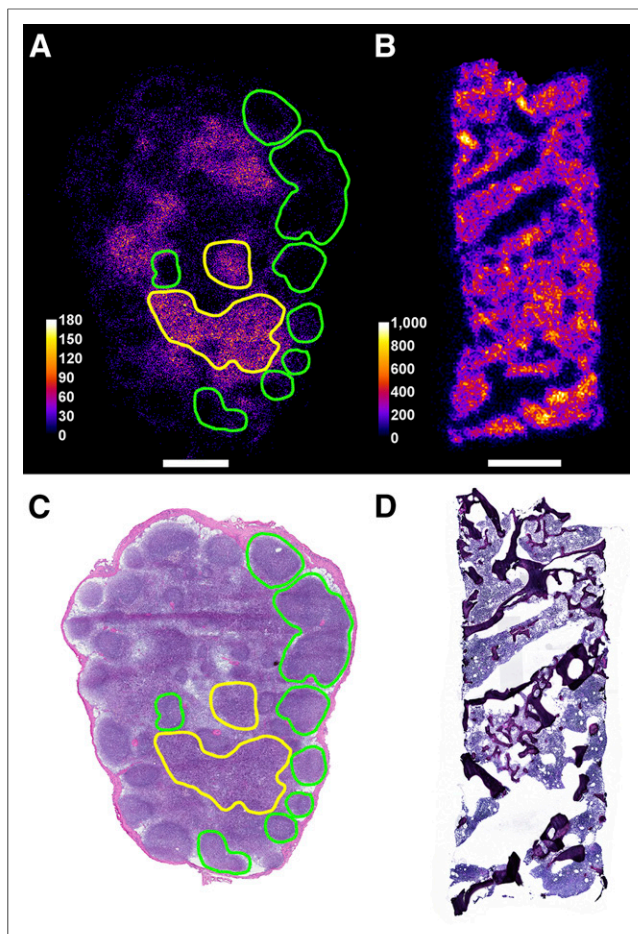


**FIGURE 2.** Distribution of  $^{211}\text{At}$  in cryosectioned tissue samples imaged using iQID camera (A and B), and corresponding H&E-stained sections (C and D). A and C show lymph node sections from dog H638, biopsied 19 h after injection; B and D show sections of bone marrow core from dog H632, biopsied 2 h after injection. Green and yellow lines indicate lymph node follicles and paracortex (including visibly apoptotic areas), respectively, identified in H&E section. Overlaid with the  $\alpha$ -image, outlined regions coincide well with low- and high-activity areas. Horizontal scale bars indicate 1 mm; color bars show  $^{211}\text{At}$  activity in microbecquerels.

than was possible with frozen samples, because of superior morphology preservation; however, few samples were large enough to enable both methods. The most comprehensive dataset was achieved for the H629 2-h biopsy seen in Figure 3. The paraffin-embedded sections were cut from the same lymph node as the  $\alpha$ -imaged cryosection in Figures 2B and 2E, albeit not consecutively. Figure 3 shows representative regions, including cortex, paracortex, and medulla, demonstrating the general morphology, T-cell localization, apoptosis markers, and macrophage localization. As expected, T cells were abundant in the paracortex but typically scarce in the cortical follicles. B-cell staining was not achieved, because of unsatisfactory antibody performance in paraffin-embedded canine tissues. Similarly, efforts to assess the distribution of CA12.10C12-B10 in untreated lymph nodes were unsuccessful. At 2 h after injection, staining for cleaved caspase-3 indicated widespread apoptosis. Macrophages containing multifocal apoptotic cellular debris were present in medullary cords and interfollicular zones, as well as within occasional germinal centers.

## Dosimetry

The absorbed dose to blood ranged from 0.013 to 0.030 Gy/MBq, corresponding to total absorbed doses of 1.6–5.7 Gy (mean, 3.1 Gy) for the mean injected  $^{211}\text{At}$  activity of 166 MBq (Table 4). Only minor intersubject variability was exhibited in absorbed dose rates to blood over time, analogous to the  $^{211}\text{At}$  blood clearance (Fig. 1B).

Concordance was seen between mean absorbed dose rates for marrow derived from either whole-tissue dosimetry of macroscopic samples (core and aspirate) or  $\alpha$ -imaging (core), ranging from 0.05–0.60 to 0.01–0.11  $\mu\text{Gy/MBq-s}$  at early and late time points, respectively (Supplemental Fig. 4A). Polynomial curve fitting of the macro biopsy data resulted in mean absorbed doses to marrow of 2.4 Gy/166 MBq. For lymph nodes, the dose rates were 0.03–0.61 and 0.01–0.20  $\mu\text{Gy/MBq-s}$  early and late, respectively (Supplemental Fig. 4B). Interestingly, two 2-h data points for dog H632 were markedly elevated, indicating rapid and high lymph node uptake of  $^{211}\text{At}$ . A polynomial fit using these two high-dose data points and the mean of all data points at 19–22 h after injection resulted in a mean absorbed dose to a high-activity lymph node of 3.4 Gy/166 MBq of  $^{211}\text{At}$ .

Figure 4 compiles the lymph node data from the 3-dimensional small-scale dosimetry for dogs H638 and H689. Highly nonuniform dose rate distributions were observed in all 3 cases (Figs. 4A, 4C, and 4D), with small hot volumes (80–180 mGy/h) dispersed in main volumes of lower dose rate levels (0–20 mGy/h). Comparison with H&E-stained sections for dog H638 (Fig. 4B) indicated colocalization of areas with high dose rate and lymphocyte-rich subregions within the lymph node.

## Toxicity

Aspartate aminotransferase levels (Supplemental Fig. 5A) remained primarily within the reference range, except for dog H632, which experienced a brief initial spike with a 2-fold increase in numbers

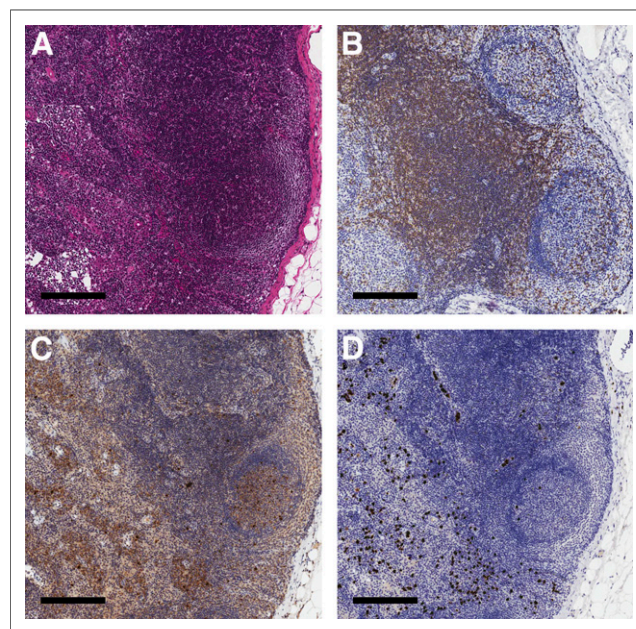


**FIGURE 3.** Immunohistochemical staining of a formalin-fixed, paraffin-embedded lymph node from dog H629, biopsied 2 h after  $^{211}\text{At}$ -B10-CA12.10C12 injection. (A) H&E-stained section, including representative areas of cortex, paracortex, and medulla. B–D show staining for T cells (CD3), apoptosis (cleaved caspase-3), and macrophages (MAC 387), respectively, in corresponding areas of serially cut sections from the same lymph node. Scale bar represents 200  $\mu\text{m}$ .



**TABLE 4**  
Mean Absorbed Dose to Blood After Injection of  $^{211}\text{At}$ -Anti-CD45 mAb

Dog no.	$^{211}\text{At}$ activity (MBq/kg)	Injected $^{211}\text{At}$ activity (A) (MBq)	Absorbed dose to blood (D) (Gy)	D/A (Gy/MBq)
H573*	14.6	112	3.3	0.030
H585*	27.6	259	5.7	0.022
H543*	11.5	147	2.2	0.015
H689*	13.9	120	1.6	0.013
H522*	13.9	165	2.5	0.015
H629†	14.6	139	2.7	0.020
H638†	18.4	227	3.0	0.013
H632†	18.7	157	3.4	0.022

\*mAb dose, 0.75 mg/kg.  
†mAb dose, 1.00 mg/kg.

above the upper limits of normal 14–28 d after HCT before returning to normal on day 42. H629 displayed a more gradual effect, with a maximum on day 136 after HCT, at which point the dog was euthanized because of severe ascites that started developing on day 119. Alkaline phosphatase levels were initially elevated (1.1–2.6 times the upper limit of normal) overall but returned to normal between days 28 and 70 after HCT, except for dog H689, whose numbers remained just above the reference range (Supplemental Fig. 5B). Bilirubin and creatinine levels were unremarkable for all dogs (Supplemental Figs. 5C and 5D).

All 6 transplanted dogs experienced transient pancytopenia (Supplemental Figs. 5E–5G). The median nadir levels for granulocytes, lymphocytes, and platelets were 9 cells/ $\mu\text{L}$  (range, 0–24 cells/ $\mu\text{L}$ ), 74 cells/ $\mu\text{L}$  (range, 57–124 cells/ $\mu\text{L}$ ), and 4,500 platelets/ $\mu\text{L}$  (range, 3,000–6,000 platelets/ $\mu\text{L}$ ), respectively, at a median time of 3 d (range, 3–5 d), 1 d (range, –1 to 2 d), and 7 d (range, 6–8 d) after HCT, respectively. The first of 3 consecutive days after nadir with absolute neutrophil counts of at least 500/ $\mu\text{L}$  occurred at a median of 9 d after HCT (range, 8–20 d), and the first of 7 consecutive days after nadir with platelet counts of at least 20,000/ $\mu\text{L}$  occurred at a median of 21 d after injection (range, 18–24 d). A median of 3 platelet transfusions were administered per dog (range, 1–6), with a transfusion threshold of 10,000/ $\mu\text{L}$ .

All dogs except H629 were euthanized in good condition after 32–48 wk of follow-up. Dogs H543, H689, H522, and H632 displayed no macroscopic or histologic evidence of toxicity in the liver, kidney, or other organs. Pathologic examination of dog H638 revealed signs of subacute bronchitis and increased iron stores in liver macrophages after 6 blood transfusions. The necropsy of dog H629 showed mild hepatic abnormalities, including features sometimes attributed to early sinusoidal obstructive syndrome. The dog's seemingly mild liver toxicity did not correspond to the level of ascites found at the time of euthanasia—a discrepancy that remains unexplained. No signs of renal toxicity were seen in any of the transplanted dogs.

## DISCUSSION

Radioimmunotherapy is a highly suitable treatment option for lymphoma because of the synergistic combination of high radiosensitivity of hematologic malignancies and accessibility of circulating radioimmunoconjugates to targets in lymph nodes, marrow,

and spleen. Our group has previously demonstrated the safety and efficacy of CD45-targeted  $\alpha$ -radioimmunotherapy in dogs as a potential substitute for external-beam total-body irradiation and high-dose systemic chemotherapy in HCT pretreatment regimens (2,3,5). The current study further assessed  $^{211}\text{At}$ -anti-CD45 radioimmunotherapy conditioning for use in upcoming therapy studies of spontaneously occurring canine lymphoma—a feasible and clinically relevant model, thanks to the many similarities to human lymphoma. Here, the administered mAb dose was optimized and the analysis was extended to include intraorgan  $^{211}\text{At}$  activity distribution and small-scale dosimetry at the micrometer range, using two  $\alpha$ -imaging techniques along with immunohistochemical staining.

The starting dose of 0.75 mg/kg proved satisfactory for targeting lymphocytes in blood and marrow but left many lymph node binding sites vacant. Increasing the dose to 1.00 mg/kg did not improve the ratios; the only significant effects were an expected

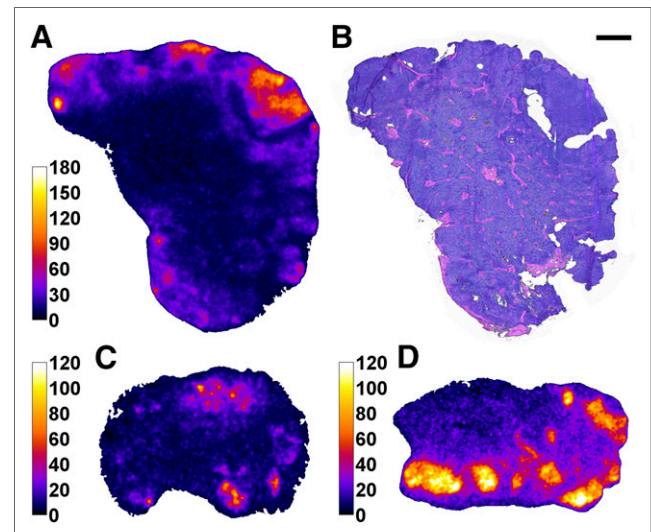


**FIGURE 4.** Dose rate images derived by 3-dimensional dosimetry using  $\alpha$ -camera imaging. (A) Dose rate distribution at biopsy for dog H638 4 h after injection. (B) Corresponding H&E-stained section. (C and D) Dose rate distribution for dog H689 2 and 19 h after injection, respectively. Color bars express dose rate in mGy/h; scale bar (top right) indicates 1 mm.

elevation in circulating anti-CD45 mAb levels and a minor shift in FMF fluorescence intensity corresponding to increased targeting of blood lymphocytes. Interestingly, the binding of fluorescein isothiocyanate-labeled anti-CD45 mAb also increased slightly; although significant, this effect was less pronounced. The results indicate that considerably higher amounts of anti-CD45 mAb likely would have been required to approach saturation in lymph nodes, causing increased nontarget irradiation by circulating radioimmunonoconjugates. Therefore, further dose escalation was not explored.

The two mAb doses generated no distinguishable differences in hematologic toxicity or hepatic/renal function, and no trends were seen in the administered  $^{211}\text{At}$  activity level. No serious toxicity was seen after administration of the lower mAb dose (0.75 mg/kg). The main adverse event was severe ascites in 1 subject 20 wk after receiving the higher mAb dose (1.00 mg/kg; 14.6 MBq  $^{211}\text{At}$ /kg) and HCT. The clinical presentation and histologic features of that dog's liver closely resembled those previously reported by our group for 2 nontransplanted dogs who were treated with  $^{211}\text{At}$ -anti-CD45 radioimmunotherapy using 0.50 mg mAb/kg (5). In that radiation dose escalation study, hepatic aberrations of clinical relevance were observed in dogs treated with more than 15.0 MBq/kg. Eight additional dogs received dog leukocyte antigen-identical marrow transplants after conditioning with a 7.5- to 23.1-MBq/kg dose of  $^{211}\text{At}$ -anti-CD45 radioimmunotherapy (0.50 mg mAb/kg), without any cases of evident liver failure. The mechanisms behind this tolerance discrepancy were not fully elucidated, but based on rat studies conducted by Harb et al. (18) it was hypothesized that radiation-induced hepatic damage may have been repaired by bone marrow-derived progenitor cells in transplanted dogs. In an earlier set of experiments, similar toxicity was seen in a dog after pretreatment with  $\alpha$ -radioimmunotherapy (326 MBq/kg of  $^{213}\text{Bi}$ -anti-CD45 mAb; 0.50 mg/kg) before dog leukocyte antigen-identical transplantation (2).

As expected, the biodistribution showed higher accumulation of  $^{211}\text{At}$  in the liver than in other nontarget organs, as is typical for radioimmunotherapy because of internalization of circulating immunoglobulins by hepatic Kupffer cells and endothelial cells (19). In addition, a slightly increased %IA/g is expected for anti-CD45-radioimmunonoconjugates because of the presence of CD45-expressing cells of hematopoietic origin in the liver (20). Even so, CD45 is attractive for radioimmunotherapy because of its abundance on target cells and its noninternalizing and nonshedding features. Most importantly, anti-CD45 mAbs do not compete with any anti-CD20 pretreatment (e.g., rituximab) for binding to target antigens, which may limit the efficacy of anti-CD20 radioimmunotherapy (21).

The estimated mean absorbed dose to blood of 3.1 Gy per 166 MBq of  $^{211}\text{At}$  was comparable to standard external total-body irradiation dose levels of 2–3 Gy (2). However, this level of absorbed dose increases markedly for  $^{211}\text{At}$ -radioimmunotherapy when one accounts for the relative biological effectiveness of  $\alpha$ -emitters, generally assumed to be in the range of 3–5 (16). Corresponding absorbed doses to marrow and lymph nodes not adjusted for relative biological effectiveness and calculated using traditional whole-tissue dosimetry were comparable to the dose to blood, but the lymph node estimations were based on a limited number of time points. Nevertheless, the dose levels of 3 Gy and above are a strong indication of satisfactory targeting, which has not been demonstrated in this model before.

$\alpha$ -imaging revealed substantial dose rate variations within the lymph nodes, but congruence between hot areas and lymphocyte-rich regions sustained the perception of effective CD45 targeting. Furthermore, markedly higher dose rates (approximately a factor

of 2) were seen in these high-activity areas at the early time points; the total absorbed dose to lymphocyte-rich target regions could thus be a factor of 2 higher than the 3.4 Gy/166 MBq that was calculated from the mean activities, should this be a characteristic time progression for each lymph node. Widespread indications of cell death observed in immunohistochemically stained sections supported the preliminary dose estimates, although more accurate dosimetry requires additional time points. Ongoing  $^{211}\text{At}$ -radioimmunotherapy studies in dogs will extend the dosimetric analysis further.

Concordance was also seen between flow cytometry data and *in vivo* activity profiles. The profuse  $^{211}\text{At}$  radioactivity registered in marrow matched the widespread targeting indicated by flow analysis; likewise, the heterogeneous activity distributions in lymph nodes corresponded well to the lower overall targeting discerned by the flow assays. CA12.10C12 supposedly targets all isoforms of CD45 expressed by T and B lymphocytes, yet our  $\alpha$ -images consistently demonstrated absence of  $^{211}\text{At}$  in B-lymphocyte-containing follicles at all studied time points. A possible explanation could be that T-cell-associated isoforms (180–220 kDa) are more abundant or easier to access than B-cell isoforms (205–220 kDa).

## CONCLUSION

Efficient targeting of  $^{211}\text{At}$ -anti-CD45 radioimmunotherapy to blood and marrow was achieved using a mAb dose of 0.75 mg/kg, without severe toxicity. Although antigen saturation was not reached, dosimetry calculations and observed radiation-induced effects in immunohistochemically stained lymph node samples indicated that sufficient  $^{211}\text{At}$  localization was achieved for use in HCT pretreatment regimens at levels of injected activity that should be tolerable for normal tissues. Our results highlight the importance of small-scale dosimetry for understanding therapeutic outcomes after  $\alpha$ -radioimmunotherapy. Ongoing studies will reveal if efficient  $^{211}\text{At}$ -B10-CA12.10C12 conditioning can be achieved for autologous HCT curative therapy of relapsed lymphoma in dogs.

## DISCLOSURE

The costs of publication of this article were defrayed in part by the payment of page charges. Therefore, and solely to indicate this fact, this article is hereby marked "advertisement" in accordance with 18 USC section 1734. Research funding was provided by National Institutes of Health (NIH) grants CA172582, CA044991, CA109663, and CA78902. The content is solely the responsibility of the authors and does not necessarily represent the official views of the NIH or its subsidiary Institutes and Centers. Sofia H.L. Frost was supported by the David and Patricia Giuliani Family Foundation and a Doug and Maggie Walker Immunotherapy Fellowship. Brian W. Miller was supported by a PNNL Linus Pauling Distinguished Postdoctoral Fellowship, developing the iQID camera in collaboration with NIH grant P41EB002035 (CGRI). No other potential conflict of interest relevant to this article was reported.

## ACKNOWLEDGMENTS

We thank the veterinarians and technicians at the canine facilities at FHCRC. Histology and immunohistochemistry was performed by Experimental Histopathology Shared Resources at FHCRC. Dr. George Sale is gratefully acknowledged for pathology support.

## REFERENCES

1. Kassis AI. Therapeutic radionuclides: biophysical and radiobiologic principles. *Semin Nucl Med.* 2008;38:358–366.
2. Sandmaier BM, Bethge WA, Wilbur DS, et al. Bismuth 213–labeled anti-CD45 radioimmunoconjugate to condition dogs for nonmyeloablative allogeneic marrow grafts. *Blood.* 2002;100:318–326.
3. Bethge WA, Wilbur DS, Storb R, et al. Radioimmunotherapy with bismuth-213 as conditioning for nonmyeloablative allogeneic hematopoietic cell transplantation in dogs: a dose deescalation study. *Transplantation.* 2004;78:352–359.
4. Nakamae H, Wilbur DS, Hamlin DK, et al. Biodistributions, myelosuppression, and toxicities in mice treated with an anti-CD45 antibody labeled with the  $\alpha$ -emitting radionuclides bismuth-213 or astatine-211. *Cancer Res.* 2009;69:2408–2415.
5. Chen Y, Kornblit B, Hamlin DK, et al. Durable donor engraftment after radioimmunotherapy using  $\alpha$ -emitter astatine-211–labeled anti-CD45 antibody for conditioning in allogeneic hematopoietic cell transplantation. *Blood.* 2012;119:1130–1138.
6. Dahlke MH, Larsen SR, Rasko JE, Schlitt HJ. The biology of CD45 and its use as a therapeutic target. *Leuk Lymphoma.* 2004;45:229–236.
7. Nakamae H, Kerbaux FR, Wilbur DS, et al. Pilot study of a  $^{213}\text{Bi}$ -labeled anti-CD45 mAb as a novel nonmyeloablative conditioning for DLA-haploidentical littermate hematopoietic transplantation. *Transplantation.* 2010;89:1336–1340.
8. Wilbur DS, Chyan MK, Nakamae H, et al. Reagents for astatination of biomolecules. 6. An intact antibody conjugated with a maleimido-closo-decaborate( $2^-$ ) reagent via sulfhydryl groups had considerably higher kidney concentrations than the same antibody conjugated with an isothiocyanato-closo-decaborate ( $2^-$ ) reagent via lysine amines. *Bioconjug Chem.* 2012;23:409–420.
9. *Guide for the Care and Use of Laboratory Animals.* 8th ed. Washington, DC: National Academy Press; 2011.
10. Storb R, Rudolph RH, Kolb HJ, et al. Marrow grafts between DL-A-matched canine littermates. *Transplantation.* 1973;15:92–100.
11. Thomas ED, LeBlond R, Graham T, Storb R. Marrow infusions in dogs given midlethal or lethal irradiation. *Radiat Res.* 1970;41:113–124.
12. Bäck T, Jacobsson L. The alpha-camera: a quantitative digital autoradiography technique using a charge-coupled device for ex vivo high-resolution bioimaging of alpha-particles. *J Nucl Med.* 2010;51:1616–1623.
13. Miller BW, Gregory SJ, Fuller ES, Barrett HH, Barber HB, Furenliid LR. The iQID camera: an ionizing-radiation quantum imaging detector. *Nucl Instrum Methods Phys Res A.* 2014;767:146–152.
14. Chouin N, Lindegren S, Frost SH, et al. Ex vivo activity quantification in micro-metastases at the cellular scale using the alpha-camera technique. *J Nucl Med.* 2013;54:1347–1353.
15. Woodward KT, Berman AR, Michaelson M, Odland LT. Plasma, erythrocyte, and whole blood volume in the normal beagle. *Am J Vet Res.* 1968;29:1935–1944.
16. Sgouros G, Roeske JC, McDevitt MR, et al. MIRD pamphlet no. 22 (abridged): radiobiology and dosimetry of alpha-particle emitters for targeted radionuclide therapy. *J Nucl Med.* 2010;51:311–328.
17. Bäck T, Chouin N, Lindegren S, Jensen H, Albertsson P, Palm S. Image-based small-scale 3D-dosimetry in targeted alpha therapy using voxel dose-point kernels and alpha camera imaging of serial tissue sections [abstract]. *J Nucl Med.* 2014;55(suppl 1):50.
18. Harb R, Xie G, Lutzko C, et al. Bone marrow progenitor cells repair rat hepatic sinusoidal endothelial cells after liver injury. *Gastroenterology.* 2009;137:704–712.
19. Johansson AG, Lovdal T, Magnusson KE, Berg T, Skogh T. Liver cell uptake and degradation of soluble immunoglobulin G immune complexes in vivo and in vitro in rats. *Hepatology.* 1996;24:169–175.
20. Li J, Xin J, Zhang L, et al. Human hepatic progenitor cells express hematopoietic cell markers CD45 and CD109. *Int J Med Sci.* 2014;11:65–79.
21. Gopal AK, Press OW, Wilbur SM, Maloney DG, Pagel JM. Rituximab blocks binding of radiolabeled anti-CD20 antibodies (Ab) but not radiolabeled anti-CD45 Ab. *Blood.* 2008;112:830–835.